Changes in Magnetic Couplings after Chimie Douce Reactions: Magnetic Structures of LiMnXO_4(OD) (X = P, As)

Miguel A. G. Aranda,*,[1] Sebastian Bruque,* J. Paul Attfield,† Fernando Palacio,‡ and
R. B. Von Dreele§

*Departamento de Química Inorgánica, Universidad de Málaga, Aptd. 59, 29071 Málaga, Spain; †Department of Chemistry,
University of Cambridge, Lensfield Road, Cambridge CB2 1EW, United Kingdom; ‡Instituto de Ciencias de Materiales de Aragón,
CSIC-Universidad de Zaragoza, 50009 Zaragoza, Spain; and §MLNSC, MSH805, Los Alamos National Laboratory, Los Alamos, New Mexico, 87545

The structural and magnetic changes that take place after the lithium exchange reactions of Mn$XO_4 \cdot D_2O$ to give LiMnXO_4(OD) (X = P, As) have been studied by magnetic susceptibility and variable-temperature neutron diffraction techniques. The crystal structures of the lithium derivatives have been refined at room temperature and 10 K by time-of-flight neutron powder diffraction data using the Rietveld method. These compounds behave as Curie–Weiss paramagnets at high temperatures and order antiferromagnetically below Néel temperatures of 28 and 30 K for X = P and As, respectively. The magnetic structures have been determined from the low-temperature neutron data. Although the four magnetic structures are antiferromagnetic, the magnetic couplings in the Mn–O–Mn infinite chains are ferromagnetic in the lithium derivatives and antiferromagnetic in the parent materials. These different magnetic behaviors are explained on the basis of subtle differences in the crystal structures after the lithium exchange reaction. © 1997 Academic Press

INTRODUCTION

First-row transition metal oxosalts exhibit a wide range of interesting magnetic properties enabling the magnetic interactions between the paramagnetic cations to be investigated. As part of this effort, the superexchange interactions between octahedrally coordinated cations have been studied in a number of transition metal phosphates and arsenates (1–4). "Chimie douce" reactions have frequently been used to modify the structural characteristics of materials which may lead to a change in properties such as electronic and ionic conductivity, catalytic behavior, and magnetic properties. For example, the Curie temperature of electrochemically intercalated $Cu_{1+y}Cr_2Se_4$ spinels varies

from 432 ($y = 0$) to 175 K ($y = 1$) (5). The loss of sample crystallinity after chimie douce reactions often makes the study of changes in crystal or magnetic structure difficult, but the compounds reported here are sufficiently crystalline to be studied by the Rietveld analysis (6, 7) of neutron powder diffraction data.

As part of a study of manganese phosphates and arsenates, we have previously shown that Mn$XO_4 \cdot H_2O$ (X = P, As) undergoes a lithium exchange reaction with solid $LiNO_3$. The ion exchange reaction of $MnAsO_4 \cdot H_2O$ to give LiMnAsO$_4$(OH) is accompanied by an unusual switch in the framework geometry as the Jahn–Teller distortions of the MnO_6 octahedra change, although the topology is unaltered (8). The structure of these two compounds consists of Jahn–Teller distorted $Mn^{III}O_6$ octahedra linked via opposite vertices by H_2O or OH^- groups to form infinite zigzag Mn–O–Mn chains in the [101] direction that are interconnected by AsO_4 tetrahedra, resulting in a three-dimensional framework. This encloses small channels parallel to the c-axis into which the hydrogen atoms are situated in $MnAsO_4 \cdot H_2O$ and in which the lithium cations are located in LiMnAsO$_4$(OH). However, after the deprotonation of the water molecules that bridge adjacent Mn^{3+} atoms, these cations become inequivalent due to the lowering of symmetry from monoclinic to triclinic. In $MnAsO_4 \cdot H_2O$ the MnO_6 octahedra are tetragonally distorted [4 + 2] while in LiMnAsO$_4$(OH) both Mn(a) and Mn(b) octahedra are better described by an orthorhombic [2 + 2 + 2] distortion.

$MnPO_4 \cdot H_2O$ is isostructural with $MnAsO_4 \cdot H_2O$, but the reaction of $MnPO_4 \cdot H_2O$ to give LiMnPO$_4$(OH) is accompanied by a different, remarkable change in the framework, as the Mn^{3+} cations are displaced to alternative octahedral sites within the PO$_4$(OH) sublattice (9). In the LiMnPO$_4$(OH) structure, the MnO_6 octahedra are also linked via opposite vertices by OH^- groups to give infinite zigzag chains, but these lie in the [001] direction. As in the

arsenate case, the structure of LiMnPO$_4$(OH) contains two inequivalent Mn^{3+} cations with an orthorhombic Jahn–Teller distortion. The structural rearrangement is due to the migration of the manganese atoms from the octahedral sites at $(1/4, 1/4, 0)$ and related positions in Mn$XO_4 \cdot$ H$_2$O to alternative octahedral holes in the channels at $(0, 0, 0)$ and equivalent positions. This change in the manganese positions gives rise to little change in the cell parameters or the coordinates of the other atoms. The vacant sites in LiMnPO$_4$(OH) are also connected to form channels that run in the [101] direction. LiMnPO$_4$(OH) has the amblygonite type structure LiAlPO$_4$(OH$_{1-x}$, F$_x$) (10). The mineral tavorite LiFePO$_4$(OH) (11) also belongs to this structure type and the magnetic properties of natural and hydrothermally synthesized samples have recently been reported (12).

We have previously reported the 4 K antiferromagnetic structures of the starting materials Mn$XO_4 \cdot$ D$_2$O (X = P, As) (14) and the magnetic structure of LiMnAsO$_4$(OD) at 10 K (15). Some ionic conductivity data for the lithium derivatives LiMnXO_4(OH) (X = P, As) have also been reported (13). In this paper we present the full crystal struc-

tures of the lithium derivatives LiMnXO_4(OH) (X = P, As) using powder neutron diffraction at room temperature and 10 K. We have also studied the changes in the magnetic properties that take place after the lithium exchange reaction using magnetic susceptibility and the low temperature powder neutron diffraction.

EXPERIMENTAL

Mn$XO_4 \cdot$ D$_2$O (X = P, As) were synthesized hydrothermally as previously described (14). LiNO$_3$ and Mn$XO_4 \cdot$ D$_2$O were ground in a 2 : 1 molar ratio and heated in a tube furnace at 200°C for 3 weeks under flowing N$_2$. The two reaction mixtures were washed with D$_2$SO$_4$/D$_2$O and D$_2$O, and dried at 60°C. Powder X-ray diffraction showed that the products were highly crystalline, single phases, LiMnXO_4(OD) (X = P, As).

Alternating current magnetic susceptibility measurements were conducted in a computer-controlled susceptometer described elsewhee (16). Data were recorded in the range 4–170 K at zero applied field. Time-of-flight neutron
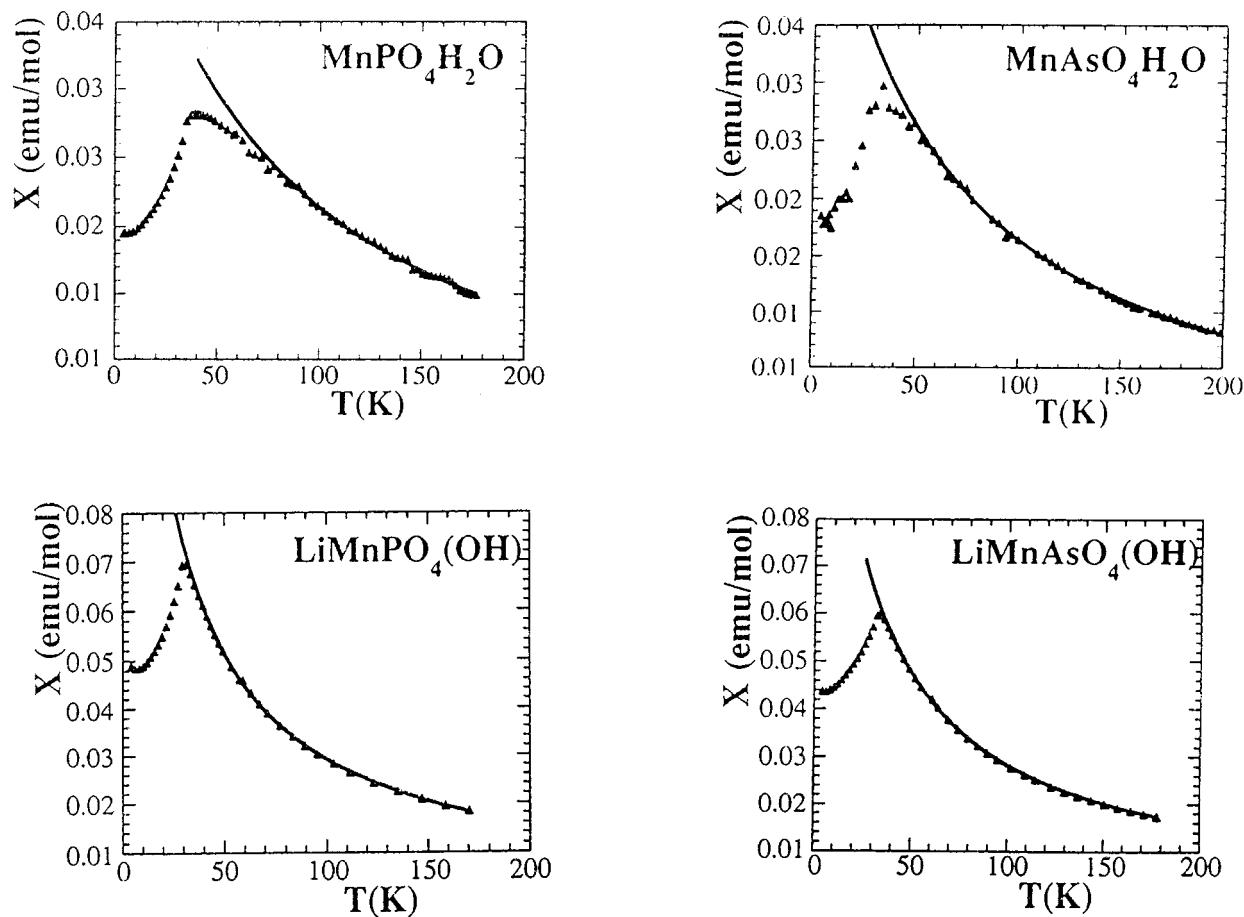

FIG. 1. Magnetic susceptibility data for Mn$XO_4 \cdot$ H$_2$O (X = P, As) and LiMnXO_4(OH) (X = P, As) between 4 and 200 K. The fitted Curie–Weiss curves are also shown.

powder diffraction patterns were collected on instrument HIPD at MLNSC, Los Alamos National Laboratory at room temperature and 10 K. The data were normalized to the incident beam spectrum and fitted by the Rietveld method (6, 7) using the GSAS package (17). Simultaneous refinements of the six spectra from counter banks at $\pm 153°$, $\pm 90°$, and $\pm 40°$ 2θ were performed with a Gaussian convoluted with a double exponential peak shape function (18) and a refined Fourier series background function. Neutron scattering lengths were taken from Koster and Yelon (19) and the Mn free ion form factor of Freeman and Watson (20) was used to calculate the magnetic intensities.

RESULTS

The crystal structures of the deuterated lithium hydroxy manganese(III) phosphate and arsenate were refined from the HIPD time-of-flight neutron powder diffraction data at room temperature using the previously determined structures (8, 9) as starting models. The positions of the lithium cations determined from laboratory X-ray powder diffraction data for the two lithium derivatives were confirmed. Difference Fourier maps clearly revealed the H/D positions. No structural changes take place on cooling from room temperature to 10 K, but magnetic diffraction peaks were clearly observed in the low-temperature neutron patterns.

The molar susceptibility data for LiMnPO$_4$(OH) and LiMnAsO$_4$(OH) are displayed in Fig. 1, together with the Curie–Weiss fits to the high-temperature data. The plots for the starting materials MnAsO$_4 \cdot$H$_2$O (X = P, As) are also given for sake of comparison (14). At low temperatures, quite sharp maxima indicative of an overall antiferromagnetic order are observed, below which the susceptibility drops to approximately 2/3 of the maximum value. Values of the Curie–Weiss parameters and transition temperatures are given in Table 1.

TABLE 1
Magnetic Susceptibility Data for LiMnXO$_4$(OH) (X = P, As)

	T_N(K)[a]	T_{max}(K)	θ(K)	μ_{eff} (μ_B) Observed	Calculated[b]
LiMnPO$_4$(OH)	28	31	− 16.2	5.2	4.9
MnPO$_4 \cdot$H$_2$O	33	40	− 63.3	5.3	4.9
LiMnAsO$_4$(OH)	30	34	− 22.6	5.2	4.9
MnAsO$_4 \cdot$H$_2$O	24	33	− 58.6	5.1	4.9

Note. The values for the starting materials (14), MnPO$_4 \cdot$H$_2$O (X = P, As), are given for comparison.

[a] Taken as the temperature of maximum slope.

[b] Assuming g = 2.00 for Mn^{3+}.

The magnetic diffraction peaks in the low-temperature neutron diffraction patterns were indexed upon the same C-centered triclinic cell that describes the nuclear structure. The magnetic reflection conditions for the LiMnPO$_4$(OD) were $h + k$ and $h + k + l$ odd and l even, and as the Mn atoms lie on special crystallographic positions, these conditions are sufficient to define the relative orientations of the four Mn spins: $(0, 0, 0) +$; $(0, 0, 1/2) +$, $(1/2, 1/2, 0) -$; $(1/2, 1/2, 1/2) -$. The reflection conditions for LiMnAsO$_4$(OD) were $h + k$ and $k + l$ odd, $h + l$ even, and this lead to the following spins arrangement: $(1/4, 1/4, 0) +$; $(3/4, 1/4, 1/2) +$; $(3/4, 3/4, 0) -$; $(1/4, 3/4, 1/2) -$ (15). For the two lithium compounds, a good fit to the magnetic intensities was obtained was obtained by refining these colinear models with magnetic components parallel to all three axes.

Final refinements of all profile and atomic parameters for LiMnXO$_4$(OD) gave the results shown in Tables 2 and 3 (X = P) and Tables 4 and 5 (X = As). Bond distances and angles are presented in Tables 6 (X = P) and 7 (X = As).

TABLE 2
Details of the LiMnPO$_4$(OD) Refinements at Room Temperature (RT) and 10 K

		+ 40°	− 40°	+ 90°	− 90°	+ 153°	− 153°	Overall
Data range (Å)		1.40–8.39	1.40–8.39	0.69–3.87	0.69–3.87	0.50–3.78	0.50–3.78	
Data range (ms)		2.5–15.0	2.5–15.0	2.5–14.0	2.5–14.0	2.5–19.0	2.5–19.0	
Residuals								
R_{WP} (%)	RT	1.9	1.7	1.8	1.8	2.3	2.3	2.0
	10 K	1.9	1.9	1.8	1.9	2.3	2.3	2.0
R_P (%)	RT	1.4	1.2	1.3	1.3	1.6	1.6	1.4
	10 K	1.4	1.3	1.2	1.4	1.6	1.6	1.4
χ^2	RT	—	—	—	—	—	—	1.7
	10 K	—	—	—	—	—	—	1.7
R_F^{nuc} (%)	RT	2.8	2.8	1.5	1.4	2.6	3.0	—
	10 K	2.5	3.0	1.1	1.6	2.1	2.1	—
R_F^{mag} (%)	10 K	3.4	3.4	5.8	4.5	9.6	8.2	—

TABLE 3
Refined Structural and Magnetic Parameters for LiMnPO$_4$(OD) in Space Group $C\bar{1}$, at Room Temperature and 10 K (Italics)

Cell data	a (Å)	b (Å)	c (Å)	α (°)	β (°)	γ (°)	V (Å^3)
	6.7186(2)	8.1866(2)	7.1232(2)	89.483(2)	117.740(2)	86.433(2)	345.77(1)
	6.7075(2)	*8.1690(2)*	*7.1194(2)*	*89.446(2)*	*117.713(2)*	*86.409(2)*	*344.34(1)*

Atomic parameters

Atom	x	y	z	U_{iso} (Å^2)
Mn(a)	0	0	0	0.05(4)
				0.03(4)
Mn(b)	0	0	1/2	0.05(−)
				0.03(−)
P	0.0236(3)	0.3501(2)	0.2356(3)	0.50(3)
	0.0242(3)	*0.3503(2)*	*0.2361(3)*	*0.22(3)*
O(1a)	0.3836(3)	0.2608(2)	− 0.1179(3)	0.57(4)
	0.3830(3)	*0.2599(2)*	*− 0.1172(2)*	*0.35(3)*
O(1b)	− 0.4735(3)	0.2420(2)	0.6066(2)	1.03(4)
	− 0.4751(2)	*0.2437(2)*	*0.6072(2)*	*0.22(3)*
O(2a)	0.3214(2)	0.0069(2)	− 0.3400(3)	0.59(4)
	0.3214(2)	*0.0066(2)*	*− 0.3393(2)*	*0.24(3)*
O(2b)	− 0.3016(2)	0.0527(2)	0.9321(3)	1.08(4)
	− 0.3012(2)	*0.0522(2)*	*0.9331(2)*	*0.53(3)*
O(3)	0.0565(3)	− 0.0947(2)	0.2774(2)	0.64(4)
	0.0576(3)	*− 0.0957(2)*	*0.2777(2)*	*0.31(4)*
Li	0.4279(10)	0.1806(7)	0.1952(8)	2.6(1)
	0.4289(9)	*0.1805(7)*	*0.1858(8)*	*1.9(1)*
D/H	0.7241(17)	0.3497(13)	0.3454(16)	1.2(3)
	0.7303(16)	*0.3541(12)*	*0.3509(16)*	*1.1(3)*

Magnetic parameters for Mn$(0,0,0)$

	Moments (μ_B)[a]				$\phi(\mu_{\mathrm{R}}, c)$ (°)[b]
	μ_{a}	μ_{b}	μ_{c}	μ_{R}	
	0.64(4)	3.40(5)	− 0.46(5)	3.46(5)	97(2)

Note. Refined occupancy of D on D/H site: 0.442(2) (at RT), 0.443(2) at 10 K.
[a] μ_{a}, μ_{b}, μ_{c}, are the magnitudes of the vector components parallel to the triclinic cell vectors a, b, and c and μ_{R} is the value of the resultant moment.
[b] $\phi(\mu_{\mathrm{R}}, c)$ is the angle between μ_{R} and the c-axis direction (Mn–O–Mn chains direction).

TABLE 4
Details of the LiMnAsO$_4$(OD) Refinements at Room Temperature (RT) and 10 K

		+ 40°	− 40°	+ 90°	− 90°	+ 153°	− 153°	Overall
Data range (Å)	RT	1.40–8.39	1.40–8.39	0.69–3.87	0.69–3.87	0.50–3.78	0.50–3.78	
Data range (ms)	RT	2.5–15.0	2.5–15.0	2.5–14.0	2.5–14.0	2.5–19.0	2.5–19.0	
Residuals								
R_{WP} (%)	RT	2.6	2.2	2.5	2.5	2.9	2.9	2.7
	10 K	2.2	1.9	2.1	2.0	2.2	2.2	2.1
R_{P} (%)	RT	1.9	1.6	1.8	1.8	2.0	2.0	1.8
	10 K	1.5	1.3	1.4	1.3	1.5	1.5	1.4
χ^2	RT	—	—	—	—	—	—	1.9
	10 K	—	—	—	—	—	—	3.7
$R_{\mathrm{F}}^{\mathrm{nuc}}$ (%)	RT	3.5	2.2	2.2	2.6	3.2	3.7	—
	10 K	3.0	1.9	1.6	1.8	2.0	2.4	—
$R_{\mathrm{F}}^{\mathrm{mag}}$ (%)	10 K	5.2	3.4	8.8	7.3	13.2	12.9	—

TABLE 5
Refined Structural and Magnetic Parameters for LiMnAsO$_4$(OD) in Space Group $C\bar{1}$, at Room Temperature and 10 K (Italics)

Cell data	a (Å)	b (Å)	c (Å)	α (°)	β (°)	γ (°)	V (Å^3)
	6.8860(3)	8.4336(3)	7.2524(3)	94.216(2)	118.152(2)	86.537(3)	370.18(2)
	6.8760(2)	*8.4147(3)*	*7.2421(3)*	*94.320(2)*	*118.114(2)*	*86.474(2)*	*368.38(3)*

Atomic parameters

Atom	x	y	z	U_{iso} (Å^2)
Mn(a)	1/4	1/4	0	0.29(5)
				0.15(4)
Mn(b)	3/4	1/4	1/2	0.29(−)
				0.15(−)
As	− 0.0386(3)	0.4046(2)	0.2429(3)	1.25(4)
	− 0.0400(2)	*0.4041(2)*	*0.2426(2)*	*0.83(2)*
O(1a)	0.4830(3)	0.1978(3)	− 0.0512(3)	1.01(5)
	0.4841(2)	*0.1967(2)*	*− 0.0507(2)*	*0.52(4)*
O(1b)	− 0.4046(3)	0.2548(2)	0.6621(3)	0.39(5)
	− 0.4051(2)	*0.2560(2)*	*0.6620(2)*	*0.27(5)*
O(2a)	0.3179(3)	0.0065(2)	− 0.4167(3)	0.79(5)
	0.3195(2)	*0.0064(1)*	*− 0.4172(2)*	*0.22(4)*
O(2b)	− 0.2359(3)	− 0.0185(2)	0.8932(3)	0.16(4)
	− 0.2355(2)	*− 0.0184(2)*	*0.8918(2)*	*0.02(3)*
O(3)	− 0.0283(3)	− 0.1624(2)	0.2812(4)	0.17(4)
	− 0.0286(2)	*− 0.1608(2)*	*0.2804(3)*	*0.15(3)*
Li	0.0154(12)	0.0548(8)	0.1953(10)	2.4(2)
	0.0104(8)	*0.0534(5)*	*0.1910(7)*	*1.3(1)*
D/H	0.3914(9)	0.3836(6)	0.3525(8)	1.9(2)
	0.3899(6)	*0.3839(4)*	*0.3553(6)*	*1.6(1)*

Magnetic parameters for Mn(1/4, 1/4, 0)

	Moments (μ_B)[a]				$\phi(\mu_R, [101])$ (°)[b]
	μ_a	μ_b	μ_c	μ_R	
	0.72(4)	3.38(5)	0.33(5)	3.48(5)	82(2)

Note. Refined occupancy of D on D/H site: 0.600(3) (at r.t.), 0.613(2) at 10 K.

[a] Magnetic moments defined as in footnote of Table 3.

[b] $\phi(\mu_R, [101])$ is the angle betwen μ_R and the [101] direction (Mn–O–Mn chains direction).

Observed, calculated, and difference plots at room temperature and 10 K are shown in Figs. 2 ($X = P$) and 3 ($X = As$).

DISCUSSION

The framework of LiMnPO$_4$(OD) and the lithium position within the channels in the [101] direction previously determined from laboratory X-ray powder data (9) have been confirmed using the room temperature neutron powder data. The D/H position (which was not located in the X-ray study) has been located. These D/H atoms are bonded to oxygen O(3) at a distance of 1.06 Å and form a strong nonlinear hydrogen bond with the O(1b) (see Table 6); the

O(3)–D/H–O(1b) angle is 167°. The sample was found to be 44% deuterated. The previously determined framework (8) of LiMnAsO$_4$(OD) has also been confirmed and the lithium position in the channels, which are parallel to the c-axis in this structure, was also corroborated. The D/H atoms are 0.97 Å from O(3) and also form a strong nonlinear hydrogen bond (see Table 7) with an O(3)–D/H–O(2a) angle 164°. This sample was also only partially deuterated containing 60%D. The 10 K crystal structures of LiMnPO$_4$(OD) and LiMnAsO$_4$(OD) do not differ from those at room temperature, except for small changes due to the thermal contraction.

LiMnPO$_4$(OD) and LiMnAsO$_4$(OD) have very similar variations of magnetic susceptibility with temperature

TABLE 6
Bond Distances (Å) and Angles (°) for LiMnPO$_4$(OD) at Room Temperature and 10 K

	RT	10 K		RT	10 K
Mn(a)–O(1a) (×2)	2.182(1)	2.186(1)	Li–O(1a)	2.197(5)	2.121(5)
Mn(a)–O(2b) (×2)	1.871(1)	1.866(1)	Li–O(1a)′	1.926(7)	1.941(6)
Mn(a)–O(3) (×2)	1.972(1)	1.972(1)	Li–O(1b)	2.745(6)	2.821(6)
Mn(b)—O(1b) (×2)	2.206(1)	2.191(1)	Li–O(2a)	2.071(6)	2.069(6)
Mn(b)–O(2a) (×2)	1.921(1)	1.919(1)	Li–O(2b)	2.169(6)	2.150(5)
Mn(b)–O(3) (×2)	1.951(2)	1.955(1)	Li–O(3)	2.054(6)	2.052(6)
P–O(1a)	1.532(2)	1.532(2)	Li ⋯ Li	2.856(11)	2.780(10)
P–O(1b)	1.521(2)	1.516(2)	O(3)–D	1.065(9)	1.076(9)
P–O(2a)	1.567(2)	1.562(2)	O(1b) ⋯ D	1.671(10)	1.673(10)
P–O(2b)	1.569(2)	1.574(2)	O(3) ⋯ O(1b)	2.719(2)	2.720(2)
O(1a)–Mn(a)–O(1a)	180	180	O(1a)–P–O(1b)	113.8(1)	113.4(1)
O(1a)–Mn(a)–O(2b)	84.2(1)	84.1(1)	O(1a)–P–O(2a)	111.4(1)	111.1(1)
O(1a)–Mn(a)–O(3)	84.8(1)	84.5(1)	O(1a)–P–O(2b)	108.6(1)	108.1(1)
O(2b)–Mn(a)–O(2b)	180	180	O(1b)–P–O(2a)	112.0(1)	112.6(1)
O(2b)–Mn(a)–O(3)	89.9(1)	89.9(1)	O(1b)–P–O(2b)	109.0(1)	109.6(1)
O(3)–Mn(a)–O(3)	180	180	O(2a)–P–O(2b)	101.2(1)	101.2(1)
O(1b)–Mn(b)–O(1b)	180	180	Mn(a)–O(1a)–P	125.1(1)	124.7(1)
O(1b)–Mn(b)–O(2a)	90.4(1)	90.5(1)	Mn(b)–O(1b)–P	136.2(1)	137.3(1)
O(1b)–Mn(b)–O(3)	96.2(1)	96.0(1)	Mn(b)–O(2a)–P	132.6(1)	132.5(1)
O(2a)–Mn(b)–O(2a)	180	180	Mn(a)–O(2b)–P	142.6(1)	142.2(1)
O(2a)–Mn(b)–O(3)	93.8(1)	93.8(1)	Mn(a)–O(3)–Mn(b)	130.5(1)	130.0(1)
O(3)–Mn(b)–O(3)	180	180	O(3)–D ⋯ O(1b)	166.7(9)	163.1(9)

TABLE 7
Bond Distances (Å) and Angles (°) for LiMnAsO$_4$(OD) at Room Temperature and 10 K

|	RT	10 K		RT	10 K
Mn(a)–O(1a) (×2)	1.833(2)	1.836(2)	Li–O(1a)	2.404(7)	2.413(5)
Mn(a)–O(2b) (×2)	2.177(2)	2.179(1)	Li–O(1b)	2.141(8)	2.134(5)
Mn(a)–O(3) (×2)	2.003(2)	2.001(2)	Li–O(2a)	2.638(7)	2.666(5)
Mn(b)–O(1b) (×2)	1.920(2)	1.919(1)	Li–O(2b)	2.128(7)	2.096(5)
Mn(b)–O(2a) (×2)	2.220(2)	2.214(1)	Li–O(2b)′	1.909(8)	1.907(5)
Mn(b)–O(3) (×2)	1.967(2)	1.973(2)	Li–O(3)	2.061(8)	2.034(5)
As–O(1a)	1.764(3)	1.756(2)	Li ⋯ Li	2.83(1)	2.79(1)
As–O(1b)	1.700(3)	1.698(2)	O(3)–D	0.969(5)	0.990(3)
As–O(2a)	1.628(2)	1.630(2)	O(2a) ⋯ D	1.887(5)	1.873(3)
As–O(2b)	1.680(3)	1.673(2)	O(3) ⋯ O(2a)	2.831(3)	2.833(2)
O(1a)–Mn(a)–O(1a)	180	180	O(1a)–As–O(1b)	98.3(1)	98.5(1)
O(1a)–Mn(a)–O(2b)	95.8(1)	95.8(1)	O(1a)–As–O(2a)	109.4(1)	109.4(1)
O(1a)–Mn(a)–O(3)	93.3(1)	93.3(1)	O(1a)–As–O(2b)	104.7(1)	104.8(1)
O(2b)–Mn(a)–O(2b)	180	180	O(1b)–As–O(2a)	112.3(1)	112.0(1)
O(2b)–Mn(a)–O(3)	95.4(1)	95.6(1)	O(1b)–As–O(2b)	112.3(2)	112.8(1)
O(3)–Mn(a)–O(3)	180	180	O(2a)–As–O(2b)	117.7(2)	117.3(1)
O(1b)–Mn(b)–O(1b)	180	180	Mn(a)–O(1a)–As	139.8(1)	139.9(1)
O(1b)–Mn(b)–O(2a)	90.2(1)	90.1(1)	Mn(b)–O(1b)–As	126.4(1)	125.8(1)
O(1b)–Mn(b)–O(3)	95.5(1)	95.5(1)	Mn(b)–O(2a)–As	130.9(1)	131.2(1)
O(2a)–Mn(b)–O(2a)	180	180	Mn(a)–O(2b)–As	122.9(1)	122.9(1)
O(2a)–Mn(b)–O(3)	98.3(1)	95.6(1)	Mn(a)–O(3)–Mn(b)	132.7(1)	132.2(1)
O(3)–Mn(b)–O(3)	180	180	O(3)–D ⋯ O(2a)	164.0(5)	162.5(3)

LiMnPO4(OD) at 300 K
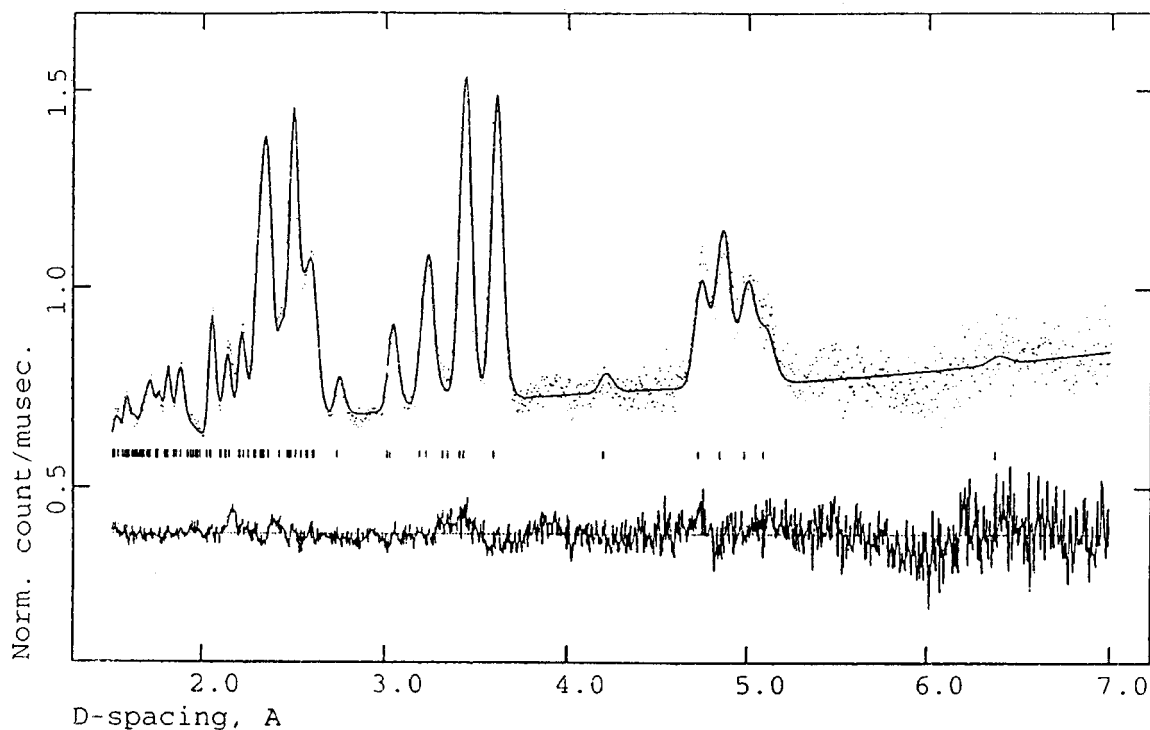
LiMnPO4(OD) at 10 K
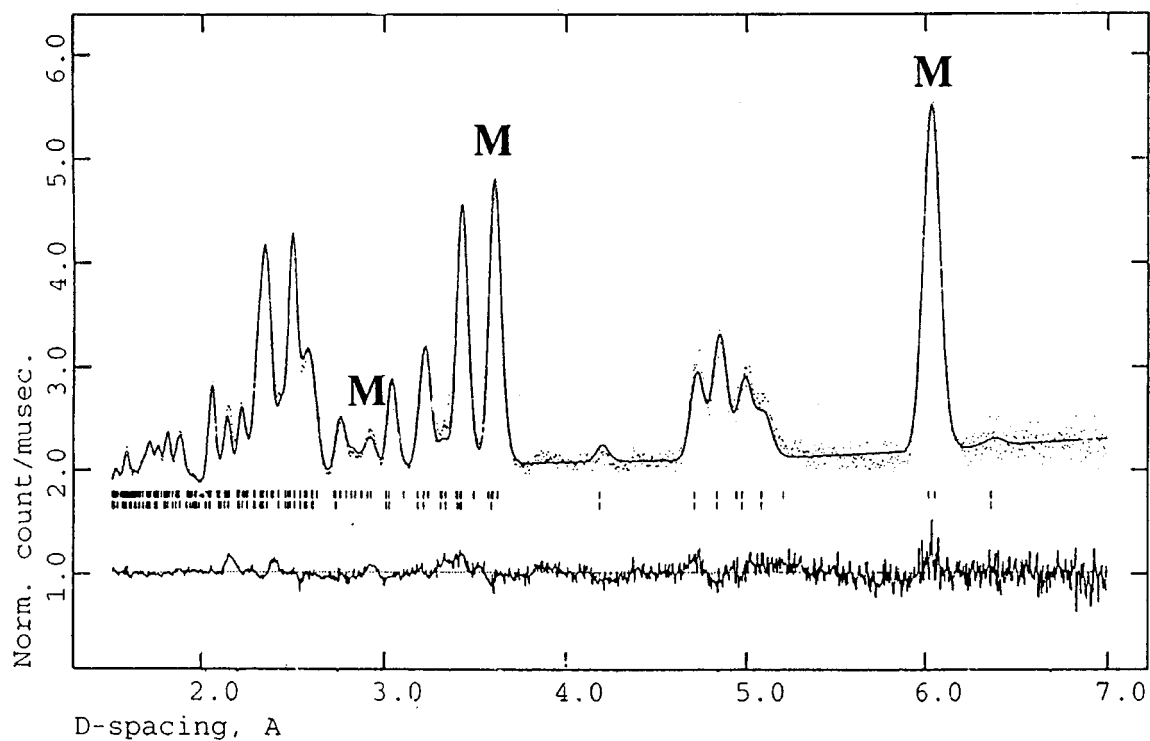
FIG. 2. Final observed (points), calculated (full line), and difference HIPD time-of-flight neutron diffraction pattern for LiMnPO4(OD) at 300 and 10 K. Only the +40° detector data are shown. The prominent magnetic peaks in the low-temperature pattern are labeled M.
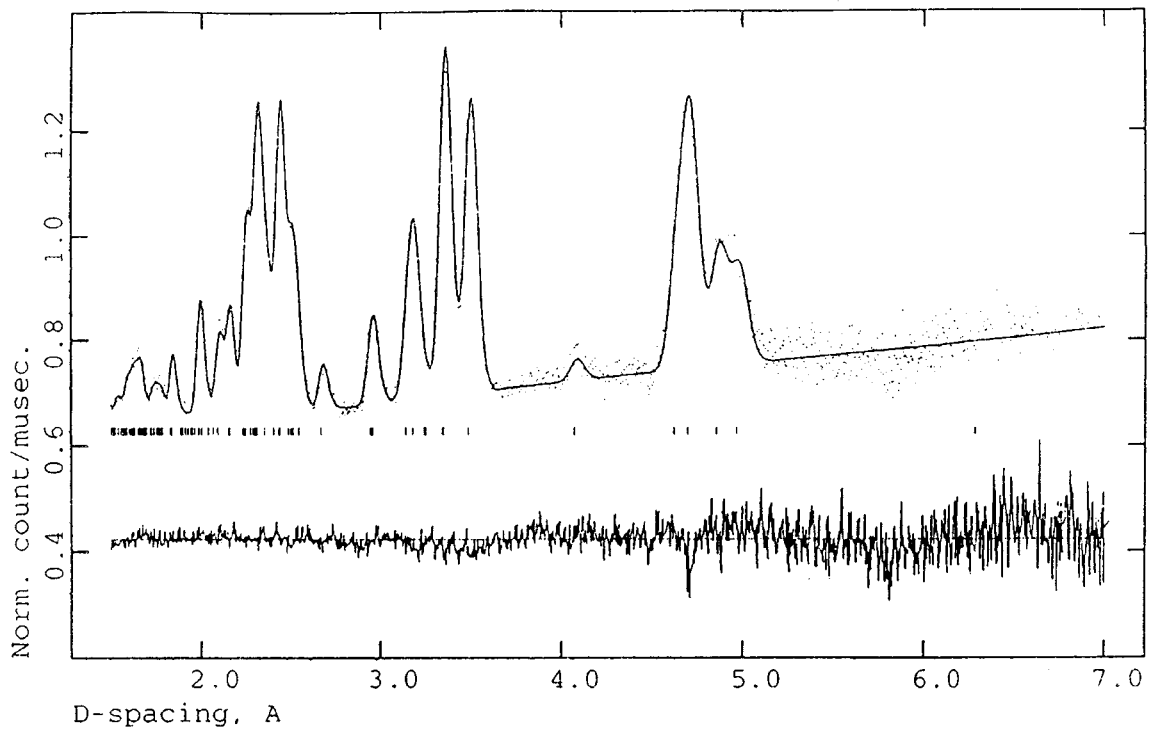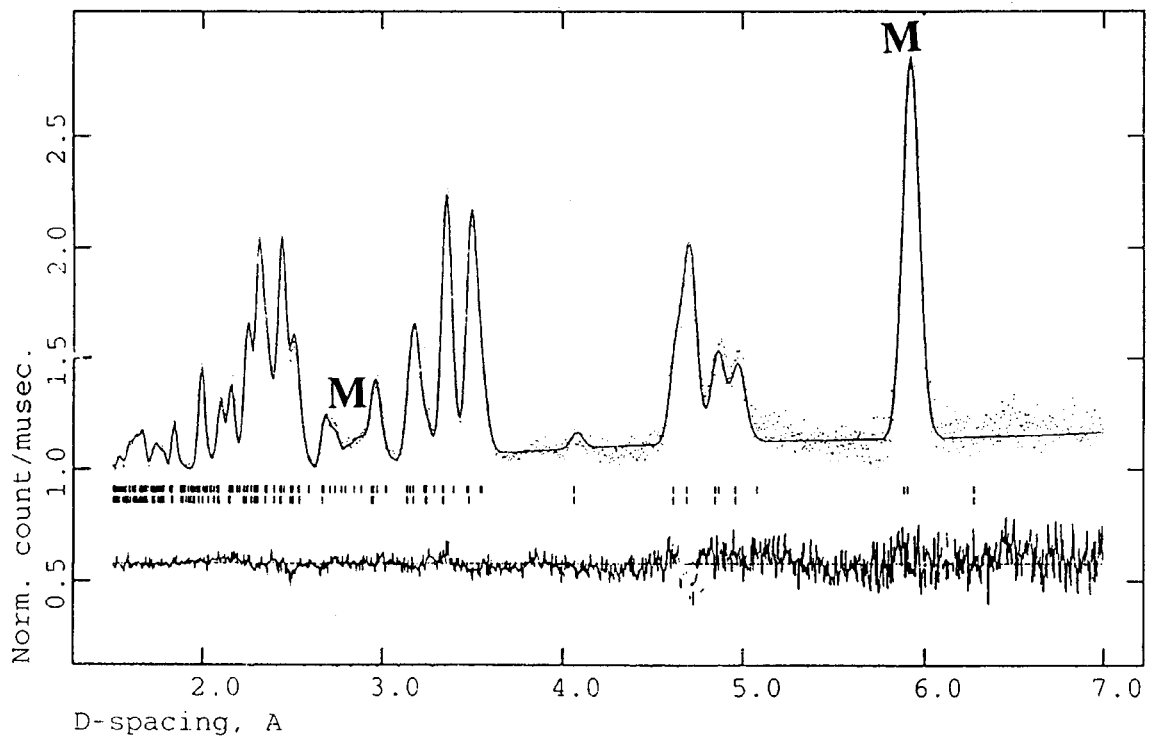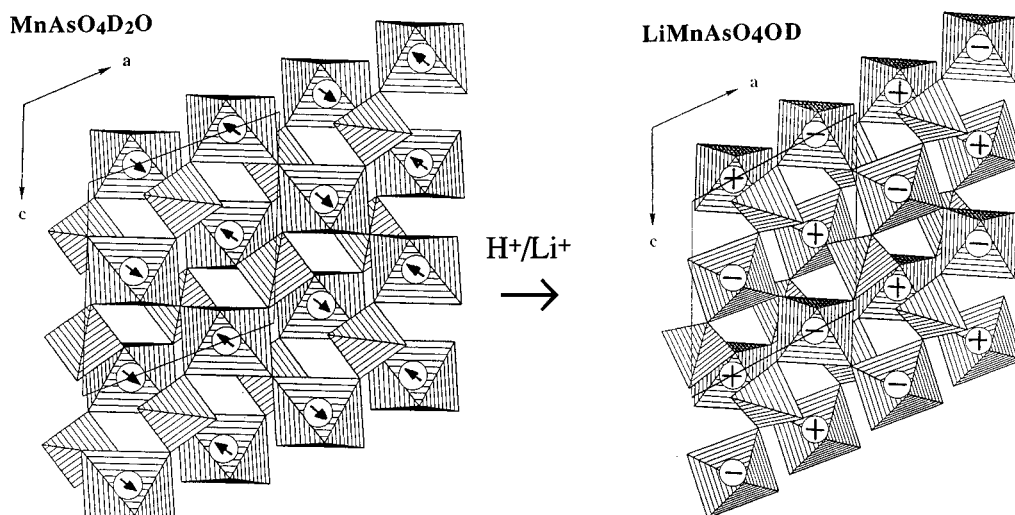
LiMnAsO$_4$(OD) at 300 K

LiMnAsO$_4$(OD) at 10 K

FIG. 3. Final observed (points), calculated (full line), and difference HIPD time-of-flight neutron diffraction pattern for LiMnAsO$_4$(OD) at 300 and 10 K. Only the $+40°$ detector data are shown. The prominent magnetic peaks in the low-temperature pattern are labeled M.

FIG. 4. Polyhedral view down the *b*-axis of MnXO$_4 \cdot$D$_2$O (X = P, As) and LiMnAsO$_4$(OD) frameworks with the change in the magnetic moments, due to the lithium exchange reaction, displayed.

(Fig. 1) giving the parameters shown in Table 1. At high temperatures they behave as Curie–Weiss paramagnets with spin-only moments and negative values of θ, indicating a dominant antiferromagnetic interaction between the spins. Both compounds display susceptibility maxima at T_{max} characteristic of long-range antiferromagnetic order and the Néel temperatures T_N were estimated from the position of maximum slope of the $\chi(T)$ curve. The sharpness of the transition and the T_N/T_{max} values of 0.90 and 0.88 for X = P and As are consistent with three-dimensional Heisenberg behavior (21). The Curie–Weiss function fits the LiMnXO$_4$ (OD) (X = P, As) data down to almost T_{max} of $\chi(T)$ curves. This indicates that although the overall magnetic structures of LiMnXO$_4$(OD) (X = P, As) are antiferromagnetics, they contain substantial ferromagnetic contributions. As seen in Fig. 1, this is an important difference with the pristine materials MnXO$_4 \cdot$D$_2$O (X = P, As) as both have broader susceptibility maxima (Fig. 1). This is supported by the magnetic structures determined from low-temperature powder neutron data, as strong antiferromagnetic Mn–O–Mn couplings are observed in the infinite chains in the MnXO$_4 \cdot$H$_2$O materials (14), but in LiMnXO$_4$(OD) (X = P, As) a weaker, ferromagnetic, intrachain coupling is present, as discussed below.

It is interesting to compare the magnetic behavior of LiMn^{III}PO$_4$(OH) and the isostructural compound tavorite, LiFe^{III}PO$_4$(OH) (12). The magnetic structure of this material is not known although the magnetic properties have been characterized through a magnetic susceptibility study. The susceptibility curve shows a very broad maximum centered at 80 K which was fitted by a one-dimensional Heisenberg model. For LiMnPO$_4$(OH), the maximum is much sharper

indicating a three-dimensional antiferromagnetic order as found in the low-temperature neutron study. The different magnetic behavior of these compounds is likely to arise from the different electronic configurations of the cations as $3d^5$Fe^{3+} forms regular coordination octahedra while $3d^4$Mn^{3+} gives rise to Jahn–Teller distortions which modify the signs and magnitudes of the superexchange pathways.

The magnetic structures of LiMnXO$_4$(OD) (X = P, As) and the MnXO$_4 \cdot$D$_2$O precursors are all antiferromagnetic and the values of the magnetic moments are all very similar (3.46(5) μ_B for LiMnPO$_4$(OD), 3.48(5) μ_B for LiMnAsO$_4$(OD), 3.52(5) μ_B for MnPO$_4 \cdot$D$_2$O, and 3.54(5) μ_B for MnAsO$_4 \cdot$D$_2$O. These are reduced from the theoretical value of 4.0 μ_B for high spin Mn^{3+} due to Mn–O covalency (22). However, there is a very important difference between the magnetic structures of the lithium derivatives and those of the parent materials. In MnXO$_4 \cdot$D$_2$O (X = P, As) the spins are antiferromagnetically coupled within the infinite Mn–O–Mn chains, whereas in LiMnXO$_4$(OD) ferromagnetic spin chains are present. Furthermore, the moments lie along the [101] chain direction in MnXO$_4 \cdot$D$_2$O, the angle between μ_R and [101] being 4(2)° for X = P and 1(2)° for X = As, but in LiMnAsO$_4$(OD), the moments are almost perpendicular to the chains and the angle between μ_R and [101] is 82(2)°. The magnetic structures of the starting material MnAsO$_4 \cdot$D$_2$O and its lithium derivative LiMnAsO$_4$(OD) are displayed in Fig. 4. Although, the crystal structure of LiMnPO$_4$(OD) does not have the same topology as the latter phase, the local environments are very similar, and again the moments are almost perpendicular to the ferromagnetic chain (*c*-axis) direction, with an angle of 97(2)° between μ_R and [001].

The switch in the intrachain magnetic interactions and the magnetic easy axis upon exchange of Li$^+$ for H$^+$ in MnXO$_4 \cdot$H$_2$O is consistent with the switch in framework geometries described previously (8, 9, 15). Octahedrally coordinated $3d^4$ Mn^{3+} is subject to a [4 + 2] Jahn–Teller distortion (Fig. 5). In MnXO$_4 \cdot$H$_2$O the long Mn–O(3) bonds are those to the water molecules that bridge the octahedra, giving infinite chains in the [101] direction. The d_{z^2} orbitals containing unpaired electrons on adjacent cations are thus directed toward the bridging oxygen atom,

enabling σ-overlap to give rise to a strong, antiferromagnetic, kinetic exchange interaction. The topotactic formation of LiMnAsO$_4$(OH) is due to the deprotonation of the water molecules bridging adjacent Mn^{3+} cations resulting in bridging hydroxide groups. The increased negative charge induces a switch of local Jahn–Teller modes, in such a way that the long Mn–O bonds associated with the d_{z^2} orbitals are now to arsenate oxygens O(2a) and σ-superexchange through the Mn–O(3)–Mn bridge is no longer possible. Superexchange can occur through weaker π-overlap of half-filled Mn orbitals with O : $2p\pi$ lobes. However, as the Mn(a)O$_6$ and Mn(b)O$_6$ octahedra are rotated by differing amounts around the Mn–O(3) bonds (the angles between the Mn(a)–O(2b) and Mn(b)–O(2a) bonds and the Mn(a)–O(3)–Mn(b) plane are 46° and 24°, respectively; see Fig. 5), the π-symmetry Mn(a) and Mn(b) orbitals are near-orthogonal, and so a ferromagnetic potential exchange interaction results.

The magnetic coupling in LiMnPO$_4$(OH) (Fig. 6) is very similar to the above case as the local geometries are very similar to those in LiMnAsO$_4$(OH). Again, σ-superexchange through the Mn–O(3)–Mn bridges cannot occur and the angles between the Mn(a)–O(1a) and Mn(b)–O(1b) bonds and the Mn(a)–O(3)–Mn(b) plane of 42° and 19° (see Fig. 5) make the π-symmetry Mn(a) and Mn(b) orbitals effectively orthogonal so that a ferromagnetic potential exchange interaction results. Thus, the switch in Jahn–Teller modes caused by the deprotonation of the MnXO$_4 \cdot$H$_2$O frameworks in forming LiMnXO$_4$(OH) also results in a switch from antiferromagnetic to ferromagnetic order within the chains of corner linked MnO$_6$ octahedra for both X = P and As. The ordering between chains which is mediated by the XO$_4$ groups is antiferromagnetic in all cases.
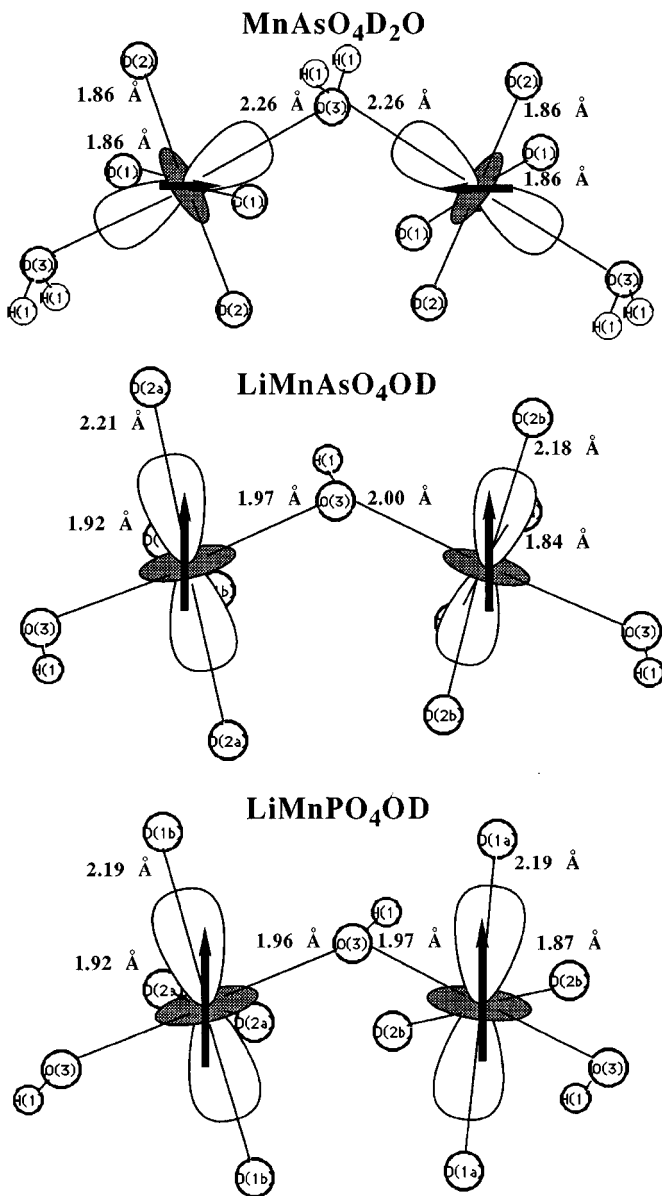

FIG. 5. Jahn–Teller distorted octahedra in MnAsO$_4 \cdot$D$_2$O, LiMn AsO$_4$(OD), and LiMnPO$_4$(OD). The bond distances and the intrachain magnetic coupling are given and the local d_{z^2}-type orbitals are also shown.
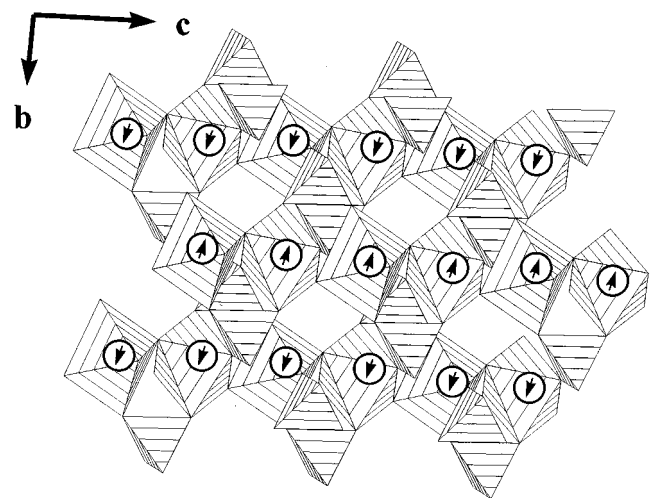

FIG. 6. Magnetic structure of LiMnPO$_4$(OD) showing the intrachain ferromagnetic coupling.

The use of intercalation and ion-exchange reactions to modify the electrical and ionic conductivities of materials is well known. This work shows the possibility of modifying magnetic properties through these types of reaction, which may allow the tailoring of new magnetic materials. In particular, the ability of host frameworks containing Jahn–Teller cations to switch between different distortion modes when exchanging or uptaking guest species may result in important changes to the magnetic properties.

REFERENCES

1. J. P. Attfield, P. D. Battle, and A. K. Cheetham, *J. Solid State Chem.* **57,** 357 (1985).
2. P. D. Battle, T. C. Gibb, G. Hu, D. C. Munro, and J. P. Attfield, *J. Solid State Chem.* **65,** 343 (1986).
3. J. P. Attfield, A. K. Cheetham, D. C. Johnson, and C. C. Torardi, *Inorg. Chem.* **26,** 3379 (1987).
4. J. P. Attfield, P. D. Battle, A. K. Cheetham, and D. C. Johnson, *Inorg. Chem.* **28,** 1207 (1989).
5. R. Schollhorn and A. Payer, *Angew. Chem. Int. Ed. Eng.* **25,** 905 (1986).
6. H. M. Rietveld, *J. Appl. Crystallogr.* **2,** 65 (1969).
7. R. A. Young (Ed), The Rietveld Method. Oxford Univ. Press, Oxford, 1993.
8. M. A. G. Aranda, J. P. Attfield, and S. Bruque, *J. Chem. Soc., Chem. Comm.* 604 (1991).
9. M. A. G. Aranda, J. P. Attfield, and S. Bruque, *Angew. Chem. Int. Ed. Eng.* **31,** 1090 (1992).
10. H. Strunz, "Mineralogische Tabellen," Akad. Verlag Leipzig, pp. 316, 1970.
11. E. A. Genkina, Y. K. Kabalov, B. A. Maksimov, and O. K. Melnikov, *Sov. Phys. Crystallogr.* **29,** 27 (1984).
12. J. L. Pizarro-Sanz, J. M. Dance, G. Villenueve, and M. I. Arriortua-Marcaida, *Mater. Lett.* **18,** 327 (1994).
13. M. A. G. Aranda, S. Bruque, J. P. Attfield, and J. R. Ramos-Barrado, *Solid State Ionics* **63–65,** 407 (1993).
14. M. A. G. Aranda, J. P. Attfield, S. Bruque, and F. Palacio, *J. Mater. Chem.* **2,** 501 (1992).
15. M. A. G. Aranda, J. P. Attfield, S. Bruque, and R. B. Von Dreele, *J. Chem. Soc., Chem. Comm.* 155 (1994).
16. C. Rillo, F. Lera, A. Bada, L. A. Angurel, J. Bartolome, F. Palacio, R. Navarro, and A. J. Van Duyneveldt, *in* "Magnetic Susceptibility of Superconductors and Other Spin Systems" (R. A. Hein, T. L. Francavilla, and D. H. Liedenberg, Eds.), pp. 124. Plenum Press, New York, 1991.
17. A. C. Larson and R. B. Von Dreele, Los Alamos National Laboratory Report No. LA-UR-86-748, 1994.
18. R. B. Von Dreele, J. D. Jorgensen, and C. G. Windsor, *J. Appl. Crystallogr.* **15,** 581 (1982).
19. L. Koster and W. B. Yelon, Summary of low energy neutron scattering wavelengths and cross sections, Netherland Energy Research Foundation, Department of Physics, Petten, 1982.
20. A. J. Freeman and R. E. Watson, *Acta Crystallogr.* **14,** 231 (1961).
21. L. J. de Jongh and A. R. Miedema, *Adv. Phys.* **23,** 1 (1974).
22. B. C. Tofield, " The Study of Covalency by Magnetic Neutron Scattering." Springer-Verlag, Berlin Heidelberg, 1975.